www.czasopisma.pan.pl PAN POLSKA AKADEMIA NAUK www.journals.pan.pl

Arch. Min. Sci. **68** (2023), 1, 141-164

Electronic version (in color) of this paper is available: http://mining.archives.pl

DOI: https://doi.org/10.24425/ams.2023.144322

KUNYOU ZHOU[1,2*], PIOTR MAŁKOWSKI[3], LINMING DOU[4], KE YANG[1], YANJIANG CHAI[4]

USING ELASTIC WAVE VELOCITY ANOMALY TO PREDICT ROCKBURST HAZARD IN COAL MINES

For the prevention and control of rockburst in underground coal mines, a detailed assessment of a rockburst hazard area is crucial. In this study, the dependence between stress and elastic wave velocity of axially-loaded coal and rock samples was tested in a laboratory. The results show that P-wave velocity in coal and rock is positively related to axial stress and can be expressed by a power function. The relationship showed that high stress and a potential rockburst area in coal mines can be determined by the elastic wave velocity anomaly assessment with passive seismic velocity tomography. The principle and implementation procedure of passive seismic velocity tomography for elastic wave velocity were introduced, and the assessment model of rockburst hazard using elastic wave velocity anomaly was built. A case study of a deep longwall panel affected by rockbursts was introduced to demonstrate the effectiveness of tomography. The rockburst prediction results by passive velocity tomography closely match the dynamic phenomenon in the field, which indicates the feasibility of elastic wave velocity anomaly for rockburst hazard prediction in coal mines.

Keywords: underground mining; rockburst hazard; stress-wave velocity relationship; elastic wave velocity; passive seismic velocity tomography; velocity anomaly

Article Highlights

(1) The dependence between stress and elastic wave velocity of axially-loaded coal and rock samples is tested in the laboratory.

[1] ANHUI UNIVERSITY OF SCIENCE AND TECHNOLOGY, SCHOOL OF MINING ENGINEERING, HUAINAN 232001, CHINA
[2] ENGINEERING LABORATORY FOR SAFE AND PRECISE COAL MINING OF ANHUI PROVINCE, HUAINAN 232001, CHINA
[3] AGH UNIVERSITY OF SCIENCE AND TECHNOLOGY, AL. MICKIEWICZA AV. 30, 30-059 KRAKOW, POLAND
[4] CHINA UNIVERSITY OF MINING AND TECHNOLOGY, SCHOOL OF MINES, XUZHOU 221116, CHINA
* Corresponding author: TB18020033B4@cumt.edu.cn

(2) A novel method of passive seismic velocity tomography for elastic wave velocity is introduced and the assessment model of rockburst hazard using elastic wave velocity anomaly is built.
(3) A case study is given to validate the feasibility using elastic wave velocity anomaly to predict rockburst hazard.

1. Introduction

As a result of long-term exploitation, coal resources at shallow depths are gradually becoming depleted, and coal mining depth is continually increasing [1]. The geological and stress conditions of the surrounding rock are becoming more and more dangerous. Mining hazards including rockbursts, gas outbursts, roof falls, etc., as well as mine roadway instabilities, are closely related to the stress states of coal and rock mass. Geological disturbances increase the rock mass stress even more [2], and the rockburst potential is higher [3,4]. Therefore, the measurement and forecast of the stress distribution in coal and rock mass are of great significance for mining safety, especially in deep coal mining, where high rock mass stress induces dynamic events and rockburst hazard [5].

Many methods are applied for rockburst hazard prediction and analysis. One can start with an overall geomechanical assessment of rock mass propensity to elastic strain accumulation and dynamic damage [6]. Then, based on geological research and making some assumptions about the rock mass, theoretical calculations [7] or numerical simulations are carried out [3,4,6,8]. However, theoretical analysis and numerical simulation always ignore the complex geological conditions and could not properly reflect stress distribution, so rock mass monitoring in roadways and panels is necessary. It can be carried out in the field using stressmetres [9] or with the help of an electromagnetic emission method [10] or an acoustic emission method [11]. But these methods are effective only to some extent because they show the local state of stress in the local environment, even if it is continuous online monitoring with a large number of probes. As portable devices, electromagnetic emission and acoustic emission gauges can detect the stress distribution in a certain area on demand, and they are more effective for rockburst hazard control. These methods are time-consuming, labour-intensive and also expensive. Geotomography is a much better solution for rock mass stress control and stress anomaly detection in underground mining.

Seismic velocity tomography, a geophysical method inferring wave propagation velocity through structures, has been widely used for years in macro-geological anomaly detection [12-14], but in recent years, it has been introduced in underground mining successfully [15-17]. Regarding seismic sources, seismic velocity tomography can be divided into two types: active and passive [18], even though active velocity tomography has been conducted in geological structures and velocity field detection in underground coal mines [19], it needs artificially triggered seismic signals, such as hammer strikes, controlled explosions etc. [20], which requires extra labour and incurs cost. Alternatively, passive tomography can display the velocity distribution using mining-induced seismicity. As a result, the geomechanical characteristics of the rock mass can be identified [21], and stress anomalies can be evaluated [17-19,22]. However, the relationship between stress and seismic wave velocity in the coal-rock configuration, as well as the detailed passive tomography procedures, is still ambiguous and rarely studied in the existing literature.

In this paper, first, a laboratory tests were conducted on the samples of coal, siltstone, coarse-grained sandstone and medium-grained sandstone to study the relationship between increased stress and corresponding wave velocity. Based on checked characteristics, the application of passive seismic velocity tomography for seismic velocity anomaly was proposed. Then, the assessment model of rockburst hazard intensity using velocity anomaly was built. Finally, the feasibility of this method was demonstrated by a field study. The accuracy and effectiveness of rockburst hazard prediction were verified by the monitoring of field rock bursts, borehole drilling and microseismicity activities.

2. Velocity-stress relationship for chosen rocks

2.1. Experimental set-up

To quantitatively determine the velocity-stress relationship for coal and rocks, 5 tests on coal and 11 tests on three other rock types: siltstone, coarse-grained sandstone and medium-grained sandstone were carried out, respectively. The rocks mentioned above are typical sedimentary rocks which surround coal seams in China, Poland, Czechia etc., so they are good examples of rock transmitting an elastic wave through the rock mass during mining and seismic event occurrences. Coal and rock samples were processed using the method recommended by the International Society for Rock Mechanics [23]. The diameter of the samples was 50 mm, and their height was 100 mm.

The measuring system (Fig. 1a) consisted of a press with a high stiff frame, a high speed camera and a seismic system. The MTS Landmark 370.50 Test System was used to load the samples uniaxially, and the loading rate was 0.05 MPa/s. The NAC GX1/3 high speed camera was used to record the deformation and failure of samples during the test. The Insite Seismic System (Fig. 1b) was used to detect the wave velocity of coal and rock samples with different stress. This system produces a pulse voltage signal from a known spatial, temporal location by a sensor (transmitter) and receives the attenuated wave by another sensor (receiver), which can then infer any changes in the coal and rock structure by calculating the transmission velocity. In

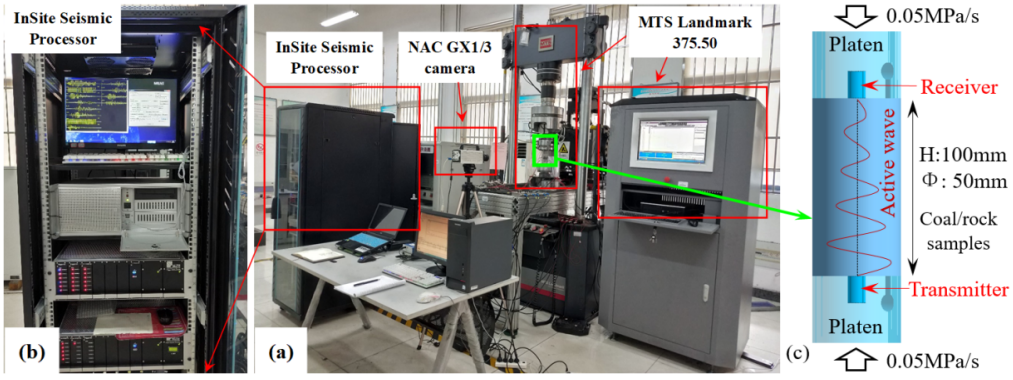

Fig. 1. Test device and measuring system. (a) Experimental system, (b) Insite seismic processor, (c) the load and sensor arrangement

this work, a transmitter and a receiver were arranged opposite each other on the two ends of the samples, as shown in Fig. 1c. The loading and measuring systems were started synchronously to record axial stress, axial strain and active signals.

The active signal had a time interval of 8-10 seconds, and a typical active wave sent by the transmitter and the corresponding attenuated wave read by the receiver are shown in Fig. 2. The frequency of the active signal was 300 kHz. The seismic wave velocity in the tested sample was calculated using Eq. (1). The homogeneous-isotropic structure of tested samples was assumed.

$$v_{est} = \frac{d}{t_{est} - t_0} \tag{1}$$

Where: d is the ray path length of 100 mm and equals to the sample height, t_{est} is the manually determined onset time of seismic wave, t_0 is the 'time zero' for the channel being processed and whilst the synthetic signal is produced.

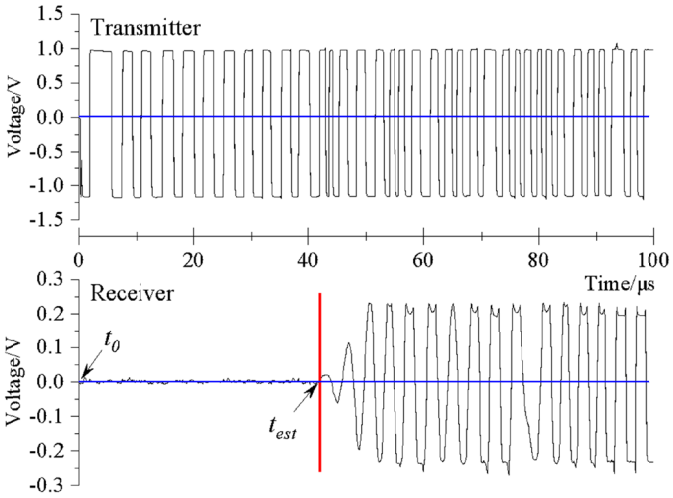

Fig. 2. The active wave by transmitter and the attenuated wave by receiver

2.2. Test results

During the uniaxial compression test, the basic mechanical parameters of compressive strength, Young modulus (tangent in the range of 30-70% of UCS) and Poisson ratio were obtained, as well as the bulk density. Additionally, the initial velocity of the elastic wave in all rocks before loading was checked. The strongest and the stiffest rock, yet heterogeneous, was medium-grained sandstone with an average UCS was 70.11 MPa, Young modulus ca. 6.3 GPa and Poisson ratio equalling 0.05. In this rock type, the initial elastic wave velocity was the highest – ca. 3922 m/s, even though the bulk density was the same as coarse-grained sandstone. The lowest average compressive strength and Young modulus were shown in coal: 16.5 MPa and 1.45 GPa, respectively, with a Poisson ratio equalling 0.17. The geomechanical parameters of the rocks tested are listed in Table 1.

TABLE 1

Primary parameters of the selected coal and rock samples

Serial number	Rock type	Bulk density [g/cm^3]	UCS [MPa]	Tangent Young modulus, [GPa]	Poisson ratio [-]	Initial velocity [m/s]
1-2	Coal	1.24	16.67	1.53	0.13	1822
1-3		1.26	17.31	1.58	0.21	2074
1-4		1.24	13.67	1.31	0.24	1639
1-6		1.25	17.30	1.40	0.11	1976
1-8		1.25	17.37	1.41	—	2109
2-1	Siltstone	2.31	20.79	2.12	0.20	2208
2-2		2.31	28.44	2.80	0.20	2422
2-3		2.38	33.93	3.01	0.22	2072
2-4		2.32	22.66	2.56	0.28	1953
3-1	Coarse-grained sandstone	2.58	30.24	4.02	0.15	3512
3-2		2.61	28.91	4.48	0.14	3621
3-3		2.55	41.38	5.05	0.11	3448
3-4		2.60	31.17	4.13	0.09	3587
4-1	Medium-grained sandstone	2.57	114.60	8.60	0.05	4303
4-2		2.55	62.48	7.14	0.05	4028
4-3		2.42	33.26	3.29	0.06	3644

Then the P-wave velocity and the stress relationship were analysed. Unfortunately due to the highly brittleness, the samples were often partly destroyed after reaching the macrodilatancy threshold and it allowed to get only some results at ultimate stress. It also did not allow any valid results from being obtained in any of the experiments after reaching the ultimate stress. The rock chips pushed the seismic sensors away during the experiment, and did not allow the relationship between stress and elastic wave velocity to be measured after the ultimate stress was applied (Fig. 3a). The sandstone samples were often cracked or crushed under the load (Fig. 3b and c).

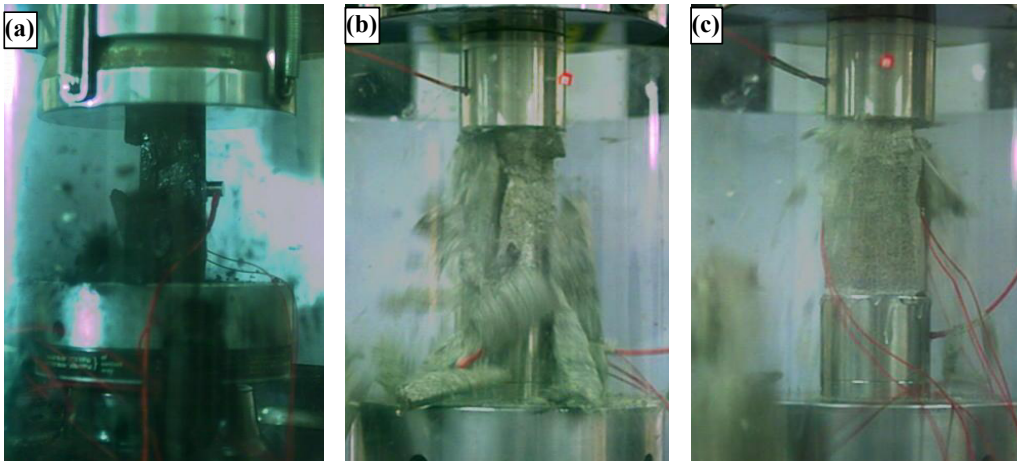

Fig. 3. The dynamic damage of sample when reaching the ultimate stress, (a) sample 1-2, (b) sample 4-4, (c) sample 5-2

To show the typical behaviour of four different tested rocks under loading, four samples were chosen to show the course of wave velocity under a given stress in Fig. 4. The analysis showed that the courses of the stress path for coal and rocks are quite similar. With increasing axial loading, all the rocks underwent fissure closure (OA – stage I), then elastic deformation took place (AB – stage II), reaching macro-dilatancy threshold at point B and quasi-plastic deformation (BC – stage III). Finally, the post-peak stage was observed (CD – stage IV). The stress course is generally identical to previous studies [24-26], but the elastic wave courses show a different manner of propagation for the chosen rocks.

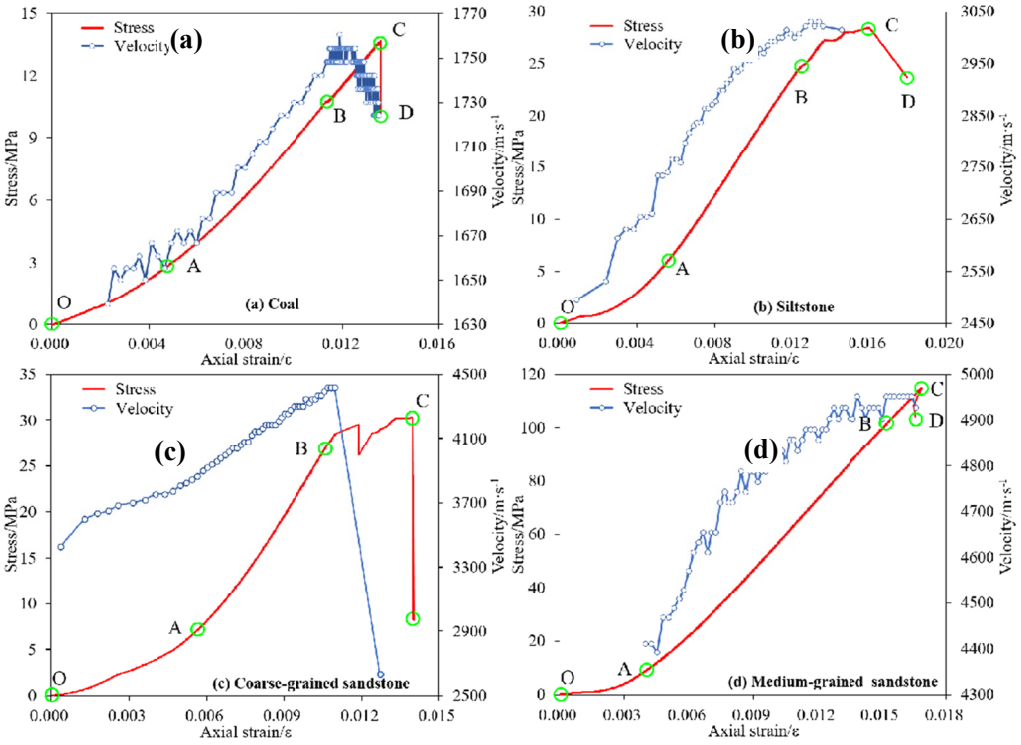

Fig. 4. Wave velocity and stress versus axial strain: (a) coal 1-4, (b) siltstone 2-2, (c) coarse-grained sandstone 3-1, (d) medium-grained sandstone 4-1

In the first stage (stage I), as a result of the increased loading, the samples are compressed, and the coal or rock particles are compacted, the P-wave velocity grows gradually due to voids in the rock structure. After void compaction, in stage II the relationship between stress and velocity is nearly linear, but the increase in the rate gradually diminishes in the latter part. In this stage, it is difficult to condense and squeeze the minerals further due to both limited space and increasing lateral deformation. In stage III, micro-cracks start to develop and this leads to structural damage. The damage is mainly characterised by the dislocation and slip of the particles, and there is almost no obvious fluctuation of the wave velocity. However, afterwards, the micro-cracks develop substantially and become macro-fractures which can be observed on the sample surface,

especially with the rock samples, which make the wave velocity decrease gradually or suddenly. This depends on rock structure and any micro-cracks developing. The most visible sudden drop was observed in coarse-grained sandstone, where relatively big grain size caused a sudden slip and breakage. Quite a smooth course of wave velocity can be observed in siltstone, where micro-crack propagation causes a slip on the surface of very small mineral particles. On the other hand, slight sudden drops in velocity were observed in the coal and medium-grained sandstone samples where micro-crack propagation behaved continuously, but the cracks periodically opened and closed. In stage IV, due to the macro-fractures and the continuing loading, the samples were macroscopically damaged, and few valid velocity data points were recorded.

It is clearly exhibited that the velocity curves of tested samples evolve similarly, and they are closely related to the strain as well as to the axial stress. Moreover, the velocity curves show distinct zoning features in different loading stages, but the wave propagation is different for the elastic and quasi-elastic behaviour of the rocks and after reaching the macro-dilatancy threshold, the velocity drops down suddenly or continuously, depending on the rock type. The highest velocity elastic wave can reach in medium-grained sandstone – 4950 m/s, then in coarse-grained sandstone – 4392 m/s, siltstone – 3237 m/s and the lowest in coal, 2202 m/s (Table 2). The given values are typical for these types of sedimentary rocks and vary according to the rock structure and mineral content. There is also a typical wave velocity increment from the initial value in a no-load state until the macro-dilatancy threshold, which can be treated as the limit of rock elasticity. The elastic limit for tested rocks was very high – in the range of 84% and 96% for coal and medium-grained sandstone, respectively (Table 2). At the elastic stage limit, the wave velocity increased by 4-6.5% in coal, 12-20% in siltstone, 7-22% in coarse-grained sandstone and 15-16% in medium-grained sandstone. Then, after reaching the elastic limit, the damage process decreased the wave velocity even below the initial value. Even though just before the moment of damage, only the wave velocity in coal and medium-grained sandstone was measured, the

TABLE 2

The change of wave velocity in rocks during their loading

Rock type	Sample no.	Stress σ [MPa]			Wave velocity v [m/s]			Wave velocity increment Δv [%]	
		Ultimate = UCS	At the elastic limit	% of UCS	Initial	At the elastic limit	At the damage	At the elastic stage limit	At the damage
Coal	1-3	17.31	16.05	92.7	2074	2164	1706	4.3	–17.7
	1-4	13.67	10.76	78.7	1639	1744	1712	6.4	4.4
	1-6	17.30	13.73	79.4	1976	2066	2057	4.5	4.1
	1-8	17.37	14.64	84.3	2109	2202	—	4.4	—
Siltstone	2-2	28.44	24.81	87.2	2507	3018	—	19.9	—
	2-3	33.93	28.69	84.6	2713	3237	—	19.3	—
	2-4	22.66	21.15	93.3	2643	2959	—	12.0	—
Coarse-grained sandstone	3-1	30.24	28.40	93.9	3597	4392	—	22.1	—
	3-2	28.91	27.47	95.0	3621	3873	—	7.0	—
	3-3	41.38	35.39	85.5	3448	—	—	—	—
Medium-grained sandstone	4-1	114.60	105.68	92.2	4303	4926	4950	14.5	15.0
	4-2	62.48	60.41	96.2	4028	4666	4644	15.8	15.3

trend was easy to observe. From the stress level control point of view, it's very important that the more compacted the rock structure is, the better it transmits the elastic wave. Even next to the damage, the wave velocity inside the loaded rock is usually still over the initial value. The same results were published by other scholars [27,28]. It proves that geotomography and wave velocity control in a rock mass can be a reasonable standard of measurement for overstressed zone positioning and rockburst control.

The velocity data in stages I and II and the corresponding stress for four tested rocks are plotted in Fig. 5. It clearly indicates that there is a positive and strong dependence between the load and P-wave velocity. With increasing axial loading, the velocity grows gradually. In contrast, its increment rate decreases simultaneously and accordingly, the relation can be expressed by a power function as Eq. (2).

$$v_p = v_0 \times \sigma^b \tag{2}$$

where v_0 is the initial velocity without loading, b is the sensitivity coefficient of the P-wave velocity to stress and σ is the current stress.

The coefficients of determination R^2 and the standard error of estimates SEE of the fitted curves and empirical relationships shown in Fig. 5 are: 0.87 and 11.13 for coal, 0.97 and 25.20

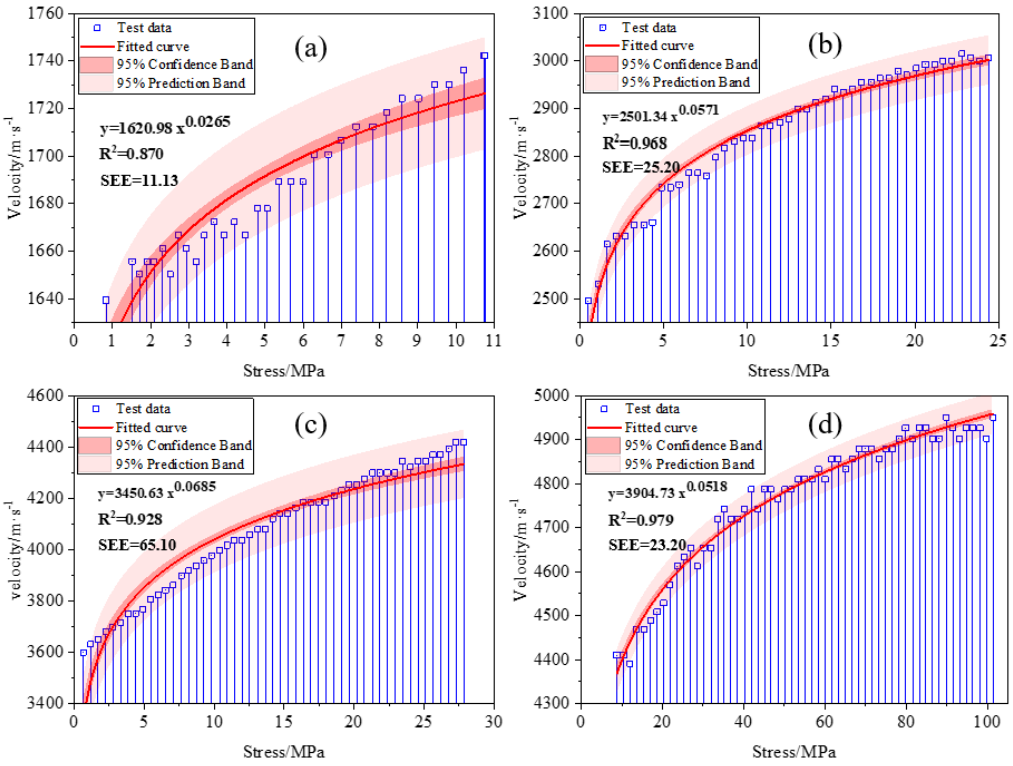

Fig. 5. The dependence between wave velocity and stress in elastic stage: (a) coal 1-4, (b) siltstone 2-2, (c) coarse-grained sandstone 3-1, (d) medium-grained sandstone 4-1

for siltstone, 0.93 and 65.10 for coarse-grained sandstone and 0.98 and 23.20 for medium-grained sandstone, respectively. So the R^2 are very high, and the SEE values are quite low. It should be underlined that all obtained results in a laboratory test are within the assumed 95% confidence band.

According to Eq. (2), the theoretical initial velocity of elastic wave in coal is 1621 m/s, 2501 m/s in siltstone, 3451 m/s in coarse sand, and 3905 m/s in medium sandstone, respectively. Comparing these numbers with the measured initial velocity (Table 2), the errors are 1.1%, 0.6%, 1.6% and 9.3%, respectively.

The velocity and variation of the inferred rocks are evidently larger than that of coal. The sensitivity coefficient b in rocks is also higher than in coal, which indicates that the rock structure is more sensitive to axial stress. This is reflected in wave velocity inside the rock body. However, when the load exceeds the elastic limit, micro-cracks – even macro-cracks – develop, and the wave propagation path breaks, and this will depress P-wave velocity significantly in any rock type, including coal.

The coefficients of determination and the initial velocity errors both confirm the feasibility of using Eq. (2) to describe the relationship between wave velocity and stress in mining practice. It has been found that the P-wave velocity in coal or rock can be significantly affected by rock type, porosity, mineral composition, homogeneity and other environmental conditions, which was underlined in the works of other scholars [29,30].

If we take into account that the siltstones and sandstones make up the majority of the carboniferous rock mass, we can infer that stress levels near the value that caused rock damage, which is reflected in an increase in elastic wave velocity of 7-20%. In the stronger rock, (in our case – medium-grained sandstone), the velocity anomaly reached a minimum of 15%, but even for not very strong fine-grained siltstones, it can be over 20%. Based on the laboratory test findings, it was confirmed that the potential high-stress and rockburst areas in coal mines can be determined by elastic wave velocity measurement and by determining its anomaly so the velocity changes in relation to the initial one. The obtained data also confirmed that an elastic wave anomaly of 15% can show an overstressed area in a rock mass, which was suggested by Dubiński (1989) [31]. Higher anomalies than 15% show the rock mass space close to damage. So, if the velocity in coal and rock mass is measured in advance, it can prevent and control rockbursts and other dynamic disasters, especially in deep coal mining. It should be underlined that a 15% seismic wave anomaly considers the rock mass to consist of different mineral rock types. For coal seams, the anomaly limit of 4% should be given.

3. Passive seismic velocity tomography for rockburst hazard

3.1. Theory of passive seismic tomography

A micro-seismic monitoring system is a widely used piece of equipment for fracture or instability monitoring of coal and rock body both accurately and in real-time [32]. It can capture and record the seismic waves with sensors around the mining area, which can be used to map the velocity distribution of the area. For passive seismic velocity tomography, the study area is divided into voxels with a certain size in x, y and z directions [20], and the seismic rays pass through the voxels along the ray path from the seismic source to the sensors.

The travel time of i^{th} seismic wave from the source to the sensor is the integral of the slowness S (or the inverse of velocity), which can be expressed by Eq. (3)-Eq. (5) [33,34].

$$v = \frac{L}{T} \rightarrow T = \frac{L}{v} \tag{3}$$

$$T = \int_0^{L_i} \frac{dL}{v(X,Y,Z)} = \int_0^{L_i} S(X,Y,Z)\,dL \tag{4}$$

$$T_i = \sum_{j=1}^{m} d_{ij} S_j \left(i = 1,2,3,...,n\right) \tag{5}$$

Where $v(X, Y, Z)$ is the seismic wave velocity (m/s) in the voxel at (X, Y, Z), L_i is the ray path length of the i^{th} seismic wave (m), T_i is the travel time from the source to the sensor (s), $S(X, Y, Z)$ is the slowness of the voxel at (X, Y, Z) (s/m), d_{ij} is the propagation distance of the i^{th} ray in the j^{th} voxel, n is the total number of rays and m is the number of voxels.

Generally, seismic event location and ray path are calculated using an initial velocity model [20]. Due to the unknown velocity, distance and time in an individual voxel, the matrices as Eq. (6) have to be built to calculate the velocity in voxels.

$$T = DS \rightarrow \mathrm{S} = D^{-1}T \tag{6}$$

where T is the travel time per ray matrix ($1 \times n$), D is the distance per ray per voxel matrix ($n \times m$), and S is the slowness per grid cell matrix ($1 \times m$).

For the calculation of slowness vector S, the most effective way is adopting an iterative process. Algebraic Reconstruction Technique (ART) and the Simultaneous Iterative Reconstructive Technique (SIRT) are the two most effective and recommended methods to do it [35,36]. In this study, SIRT is adopted for better convergence and accuracy of tomography results [18,22].

It is well acknowledged that the wave in rock mass will develop into two types, i.e. P-wave and S-wave, and P-wave propagates faster than S-wave. With increasing transmission distance, the arrival time interval of the P-wave and S-wave increases and the P-wave and S-wave will be more distinguished [33]. However, for mining-induced tremors monitoring in a particular coal mine, the wave transmission distance is limited. The S-wave arrival time always hides in the tail of the P-wave and is hard to be determined. A typical wave of the mining-induced tremors is shown in Fig. 6. Hence, in this work, the P-wave onset time of a seismic wave was picked, and the P-wave velocity was used in the tomography because it can be clearly distinguished and enables accurate results.

3.2. Rockburst hazard geotomography

Passive seismic velocity tomography for rockburst hazard control, also called: passive geotomography, can be realised with the steps shown in Fig. 7:

(i) A micro-seismic monitoring system is installed in the target area, and the sensor number and location are optimised. Mining-induced tremors are recorded, and the P-wave onset time of seismic wave (P_p) is picked manually.

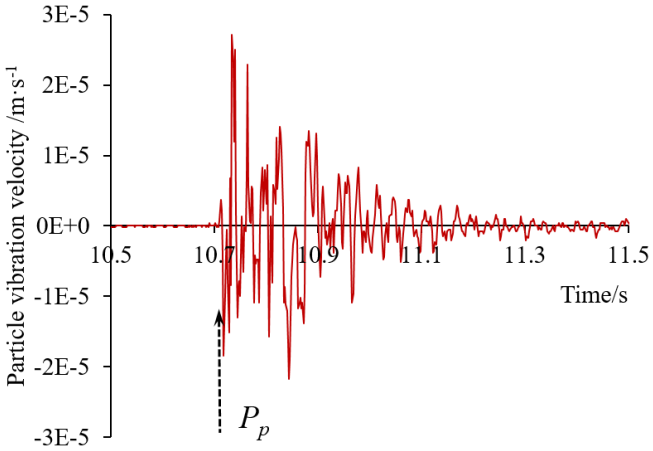

Fig. 6. A typical wave of mining-induced seismicity

(ii) The target area is divided into voxels with certain sizes in X, Y and Z directions. The initial tremor location is determined, and the wave velocity is calculated using a constant velocity model in which the seismic wave is assumed to propagate from the seismic source to the sensor linearly, and the voxels on a certain ray path are of the same seismic velocity. To avoid indeterminacy, a uniform initial velocity is assigned to each voxel and moreover, the velocity range of voxels is limited to a certain scale, which can be determined by field statistics and experimental results. Then an initial velocity model is built.

(iii) Based on the initial velocity model determined in (ii), a ray tracing method including the ray bending method, the minimum time path method and the hybrid method [36] is chosen and adopted accordingly to distinguish ray paths.

(iv) The tremor locations are then optimised using the GE-POWELL algorithm [33,36], and the theoretical arrival time of the P-wave of all rays (P_t) are calculated. Then, the residual time between the P_p in (i) and the P_T of each ray is calculated successively. Afterwards, the residual error of the model (E_{re}) is determined using Eq. (7).

$$E_{re} = \sqrt{\sum_{i=1}^{n} \left(P_{ti} - P_{pi} \right)^2} \tag{7}$$

Where P_{ti} and P_{pi} are the theoretical and measured arrival time of the i^{th} ray, respectively, n is the total amount of the rays in the velocity model.

(v) If the E_{re} is larger than the critical value (E_{cr}), SIRT is used to optimise the previous velocity model in which the slowness of all voxels with regards to all the passing rays are modified [20] and then steps (iii) and (iv) are repeated until the E_{re} is less than E_{cr}.

(vi) If the E_{re} is less than E_{cr}, the optimal velocity model is obtained. The ray density and seismic velocity of voxels are determined. A higher ray density enables higher inversion accuracy, and only the seismic velocity of the voxels with more ray density (D_r) than the critical value (D_{cr}) is reliable.

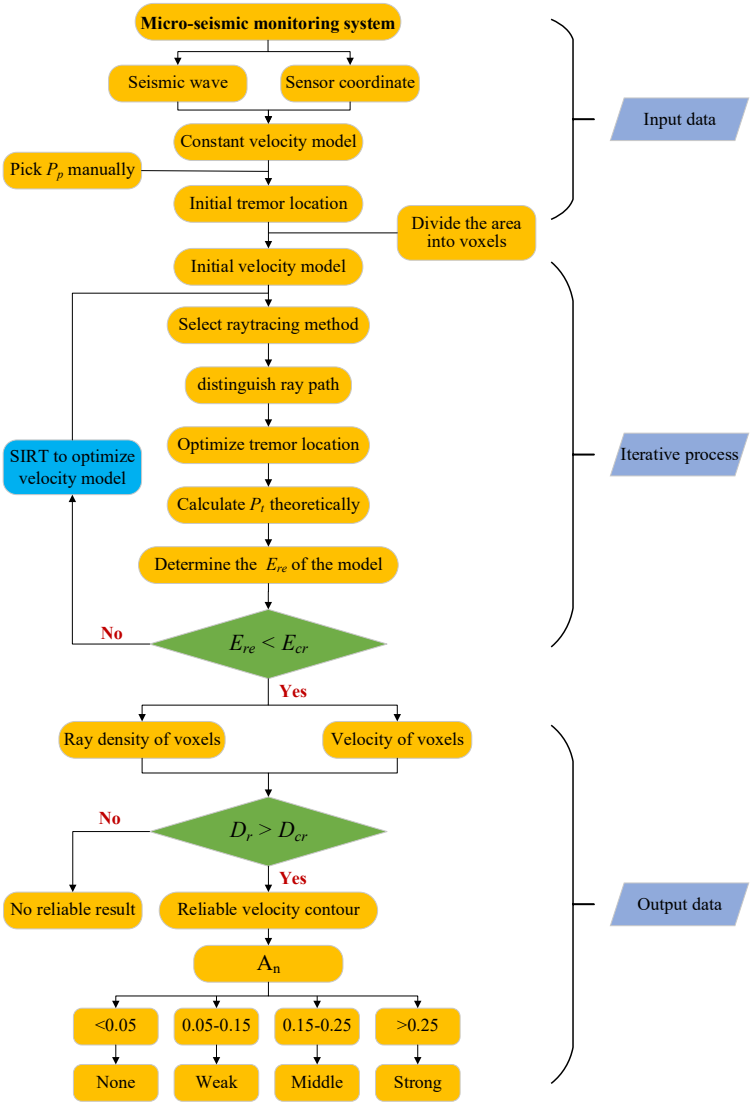

Fig. 7. Flow chart of passive seismic velocity tomography for a rockburst hazard

(vii) With seismic velocity of the reliable zones in (vi), an assessment model of rockburst hazard using velocity anomaly can be built. Where the velocity anomaly A_n is calculated according to Eq. (8).

$$A_n = \frac{v - v^a}{v} \tag{8}$$

Where v is wave velocity in voxels, and v^a is the average velocity of the voxels with the same z level.

In the assessment model, the velocity anomaly A_n is divided into four classes (Table 3), where the corresponding rockburst hazard is given, described as: none, weak, middle and strong; and the possible stress increment is suggested as well [31,33,37]. Finally, in the controlled rock mass space, the rockburst hazard area can be determined, showing velocity anomaly contour, which is fitted using a different algorithm.

It should be noticed that rockburst hazard criteria consider typical carboniferous rock mass consisting of mineral rocks. As laboratory tests showed, the rockburst hazard level in coal seams (the seam rockbursts) should have other values of seismic wave anomaly. Moreover, the local geological conditions can cause higher seismic anomalies, but they can be successfully analysed together with the *b-value* of the Gutenberg-Richter relationship or energy index *EI* developed by Van Aswegen and Butler [38].

TABLE 3

Rockburst hazard increase ratings based on seismic anomaly (Dubiński 1989)

Stress increase rate	Rockburst hazard level	Seismic anomaly A_n [%]	Rock mass stress increase [%]
0	None	<5%	<20
1	Low	5 to 15	20 to 60
2	Medium	15 to 25	60 to 140
3	High	>25	>140

4. A case study

The case study comes from the mining district No 2 in a coal mine seriously threatened by tremors and rockbursts in Shaanxi Province, China. The analysed longwall panel, number 204, was the fourth fully mechanised caving longwall face in the field. Its length was 1455 m in the strike direction and the width – 200 m in the dip direction, as shown in Fig. 8. The mined No. 4 coal seam had a thickness of 5.9-15.0 m and a dip angle of 0-15°. The average depth of mining works was 950 m. Number 4 coal seam is of medium/strong burst propensity, but the rock strata in the floor and roof are both of weak burst propensity. The average elastic energy index, bursting energy index and dynamic failure time for coal [39] were 13.36, 3.20, and 278.40 ms, respectively. The bending energy indexes for roof and floor rocks were 54.52 kJ and 20.08 kJ. The in-situ stress was measured with the stress relieving method at roadways in the points shown in Fig. 8, and the maximum principal stress with the value of 38.2-44.8 MPa had the horizontal position along the longwall panel length. Hence, coal seam number 4 was exposed to very high stress. Therefore, the stress measurement ahead of the face line was of great significance for the prevention and control of a rockburst hazard in panel 204. Moreover, this particular longwall face advance was slow – ca. 65 m/month. The face line on 20th September 2019 was 560 m, and on 30th May 2020 was 1080 m from the open-off cut, as shown in Fig. 8.

The daily amount of mining-induced events ranged from 4 to 212 with a mean of 28, which was closely related to the coal mining operation, including panel advancing speed, panel location, etc. During the chosen period of time, 11370 tremors were recorded, and their energy and the corresponding number are shown in Table 4.

A micro-seismic monitoring system called “SOS” was introduced by The Central Mining Institute in Poland and was installed underground in the mine and next to panel 204. The location

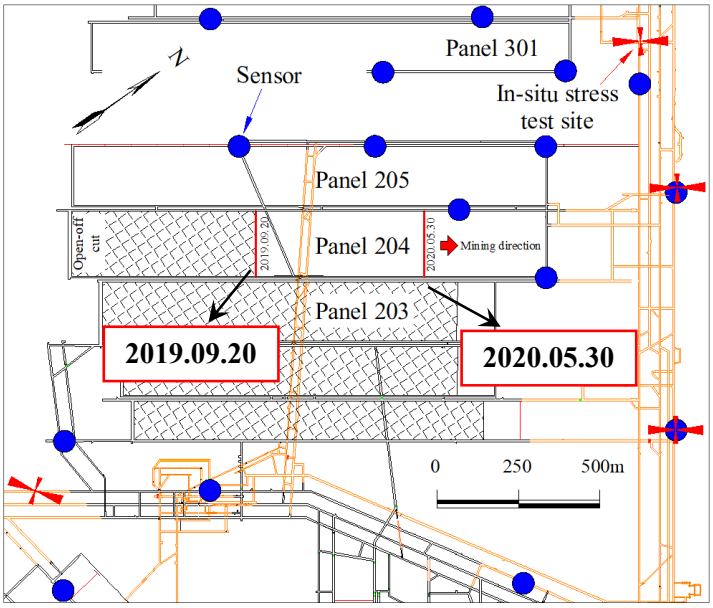

Fig. 8. Layout of "SOS" sensors in May 2020, panel location on 20th September 2019 and 30th May 2020

TABLE 4

Mining-induced tremors in mining district No 2 from 20th September 2019 and 30th May 2020

Energy [J]	$0\text{-}10^2$	$10^2\text{-}10^3$	$10^3\text{-}10^4$	$10^4\text{-}10^5$	$10^5\text{-}10^6$	$10^6\text{-}10^7$
Number of events	410	3139	5835	1793	184	9

of sensors was optimised with panel advancement. The sensors layout in May 2020 is shown in Fig. 8 (blue dots). The coal retreating area in panel 204 was surrounded by the sensors of "SOS", and the mining-induced tremors could be recorded effectively.

As an initial velocity model close to the true model can enable a quicker iterative process and a reliable tomography result [20,36], the P-wave arrival time of the mining-induced seismic signals in panel 204 was picked manually (as shown in Fig. 9). The initial P-wave velocity was obtained using a constant velocity model, it is calculated by the linear distance between the seismic source and sensor divided by the P-wave arrival time. To decrease the error of locating mining-induced tremors, the events recorded by less than six receivers were omitted. The frequency of the mining-induced signals was 0-250 Hz, and the higher the tremor energy was, the lower its frequency was.

The histogram of the registered P-wave velocity is shown in Fig. 10. P-wave velocity ranged from 3.0 km/s to 8.0 km/s, and the average velocity was 4.48 km/s, respectively. Additionally, 95% of registered wave velocities were between 3.5 km/s and 6.5 km/s. Therefore, the initial velocity of all voxels in the initial velocity model was assumed as 4.48 km/s, and in an optimised velocity model for the analysis, the wave velocity was limited to 3.5-6.5 km/s.

In geotomography, the voxel size was 30 m, 30 m and 20 m in *X*, *Y* and *Z* directions, and 60, 60 and 20 voxels in *X*, *Y* and *Z* directions were used, respectively. The ray bending method

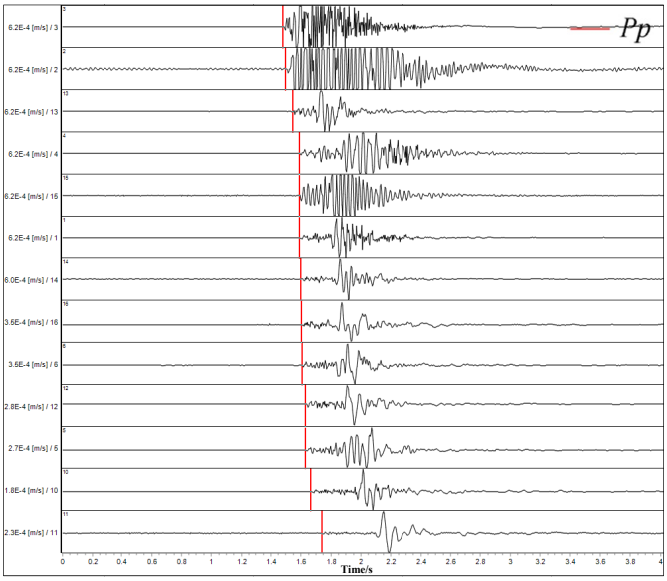

Fig. 9. P-wave arrival time pickup of registered mining induced tremor in panel 204

(a ray tracing method) was adopted, and then, a passive seismic velocity tomography was carried out with the steps described in Fig. 7. The ray bending algorithm aims to iteratively resolve the linear ray path between the seismic source and sensor, and constantly increases the number of non-collinear connection segments until the travel time along the non-collinear ray path reaching a stable yet low value. A higher ray density enables a higher inversion accuracy in this study. The velocity in the voxels obtained based on more than 15 rays was considered reliable.

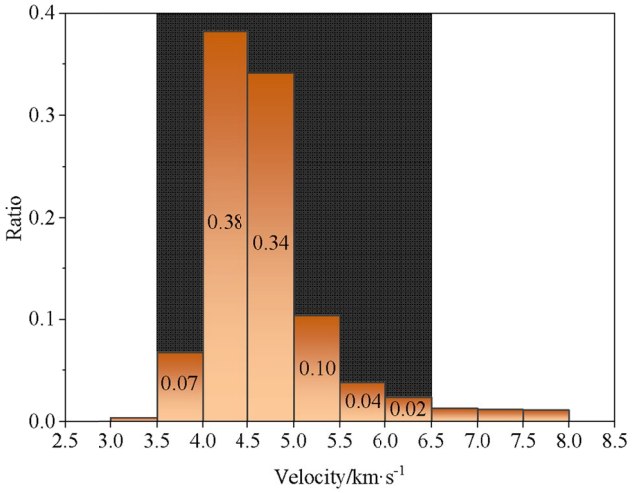

Fig. 10. P-wave velocity histogram

5. Results and discussion

5.1. Tomography results

The first passive tomography was conducted from 5th September 2019 to 20th September 2019. The 162 mining-induced tremors and 1332 seismic rays in the tomography were then recorded. The residual error E_{re} during iteration was 3.14 ms, as it is shown in Fig. 11.

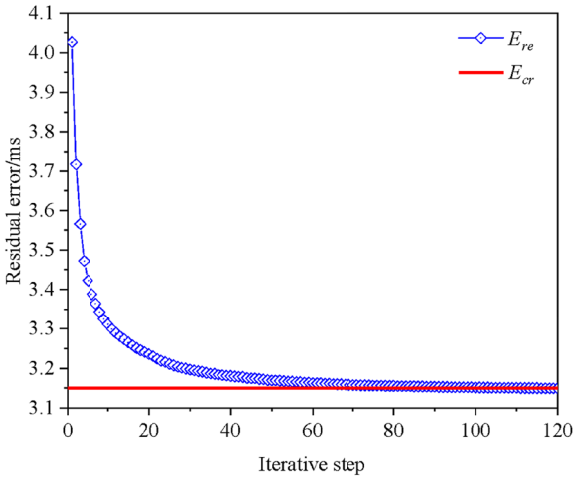

Fig. 11. Ere of the tomography on 20th September 2019

The tomography results and the future mining-induced tremors, which took place from 21th-26th September 2019, are illustrated in Fig. 12. The ray density means the seismic ray number passing through each voxel, and the v and A_n mean the seismic velocity and velocity anomaly, respectively. It can be clearly seen that the potential rockburst areas predicted by the tomography mainly lie in three subareas:

- Subarea I – located in longwall panel 205 above the headentry, the maximum velocity anomaly was 0.34, which shows a strong rockburst hazard. For headentry, the influence range was 0-130 m ahead of the face line in the strike direction.
- Subarea II mainly lays in the middle of panel 204, 40-270 m ahead of the face line in the strike direction. The maximum velocity anomaly of 0.33 was similar to the maximum value in the first subarea, and it also showed strong anomaly and high rockburst hazard risk. For tailentry, the influence range was 140-230 m ahead of the face line in the strike direction.
- Subarea III mainly lays beside the headentry. The maximum velocity anomaly was 0.31 and indicated the strong rockburst hazard. For headentry, the influence range was 250-460 m ahead of the face line in the strike direction.

The mining-induced tremors on 21st-26th September 2019 were almost all registered in Subarea I and II, so microseismic activity matched the tomography results. A rockburst occurred

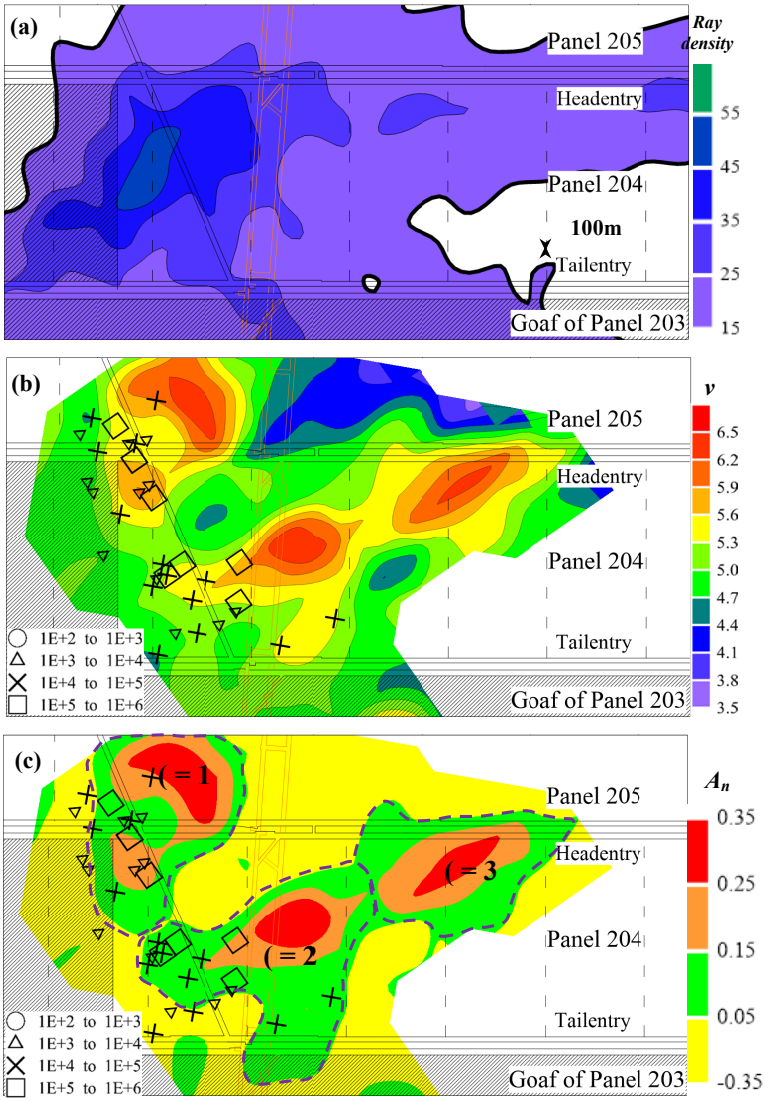

Fig. 12. Tomography results from 20th September and future tremors layout registered in the period of 21th-26th September 2019; (a) ray density distribution, (b) velocity distribution (v), (c) velocity anomaly distribution (A_n)

on 21st September 2019, and then a tremor of 4.6×10^5 J was recorded at 18 m in front of the face line on the headentry side, as shown in Fig. 13. The headentry section between 20 m and 140 m in front of the face line was damaged (Fig. 13). The total uplift of about 1.5 m of the headentry floor, 60-100 m ahead of the face line, was recorded and the working cross-section decreased sharply, which led to a 4-day shutdown of longwall panel 204. The rockburst and the damaged zone appeared in the rockburst hazard area in Subarea I, and this confirmed the tomography results.

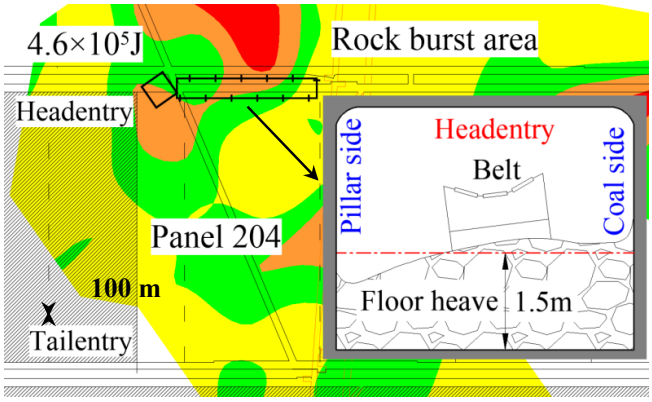

Fig. 13. Rock burst area on 21th September 2019

The second passive tomography was applied from 26th May 2020 to 30th May 2020. During this period, 974 mining-induced tremors and 5881 seismic rays were recorded. The residual error E_{re} obtained during iteration finally reached 2.39 ms, as shown in Fig. 14.

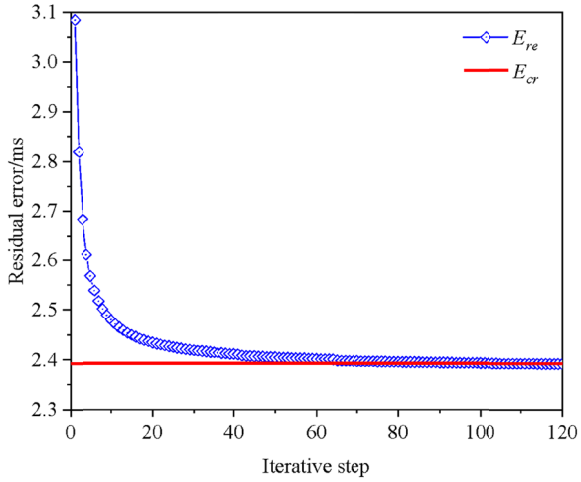

Fig. 14. E_{re} of the tomography on 30th May 2019

The tomography results from 30th May and the future mining-induced tremors during 1st -2nd June 2020 are illustrated in Fig. 15, and it indicated that rockburst hazard areas were mainly distributed in two subareas:

- Subarea I in the middle of panel 204 in the dip direction. It was 120 m behind and 130 m ahead of the face line in the strike direction. The maximum velocity anomaly was 0.20, and it showed the middle rockburst hazard. For headentry, the influence range was 0-130 m ahead of the face line in the strike direction.

- Subarea II laying next to the headentry inside longwall panel 204 and in an area 180-330 m ahead of the face line in the strike direction. The maximum velocity anomaly was 0.22, which again showed medium stress increase and middle rockburst hazard. For the headentry, the influence range was 190-290 m ahead of the face line in the strike direction.

Mining-induced tremors were registered on 31st May and 1st June 2020. The energy recorded, mostly between 1×10^3-9×10^5 J, were almost all located in Subareas I and II (Fig. 15). In this case, seismic activity and the tomography results were once again well matched.

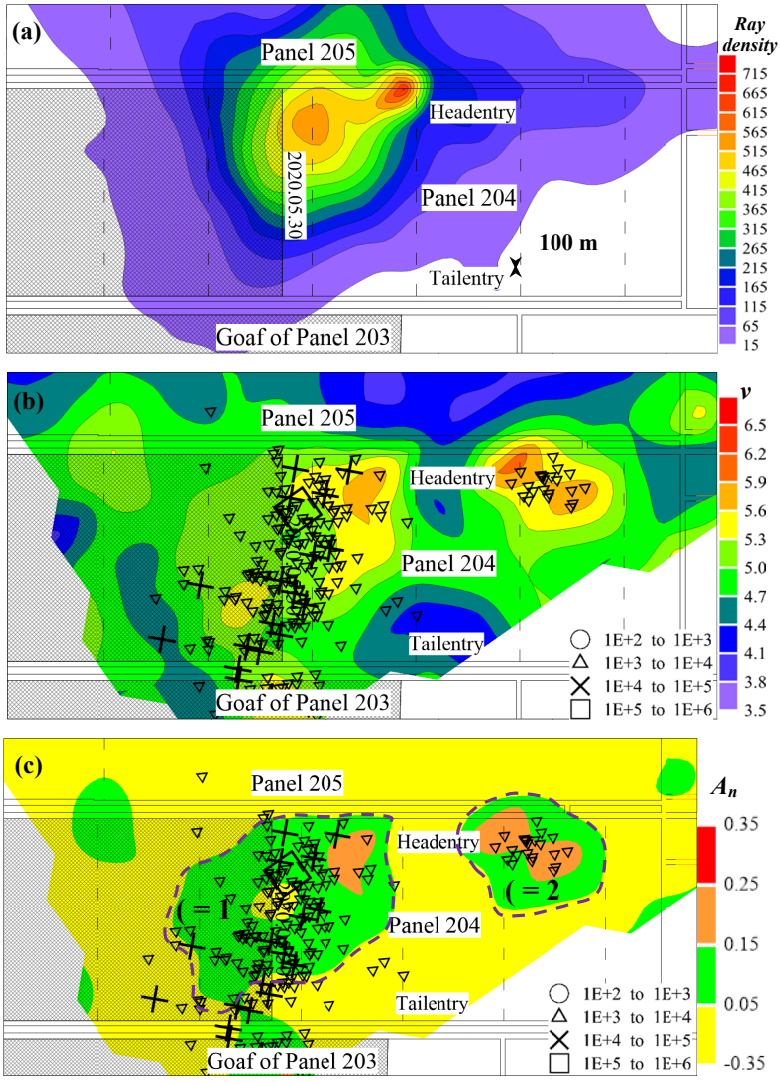

Fig. 15. Tomography results on 30th May and future tremors on 31st May-1st June 2020. (a) ray density distribution, (b) velocity distribution (v), (c) velocity anomaly distribution (A_n)

Subarea II was 180 m from the face line and outside the advanced abutment pressure area. The partially enlarged contour of subarea II is shown in Fig. 16. To relieve the coal stress, in Subarea II from 31st May-1st June 2020, two sets of large diameter boreholes were drilled, and the borehole numbers were 8 and 14, respectively. The boreholes were vertical to the coal wall in the headentry, and they were 153 mm in diameter, 30 m in depth and 1m in the interval. Unlike in other areas, during borehole drilling in Subarea II, intensive coal cannons occurred frequently, and numerous tremors with energies up to 6×10^4 J were recorded, as shown in Fig. 16. It indicated high stress in the rock mass and high rockburst hazard in Subarea II.

In this case, the layout of the borehole drilling-induced tremors and the rockburst hazard area detected by passive tomography matched well with each other, and the results of geotomography were very helpful in rockburst hazard prediction.

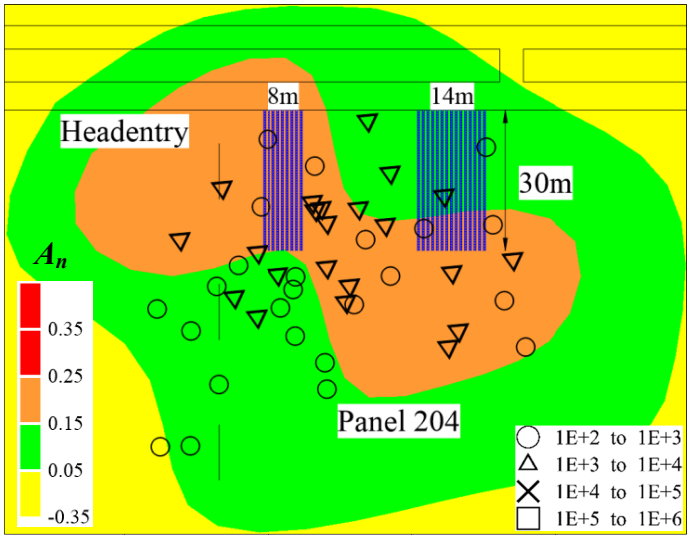

Fig. 16. Large-diameter boreholes layout in Subarea II

5.2. Discussion

Dynamic disasters in underground coal mining, including rockbursts and outbursts, are caused by the superposition of both static load and dynamic load [40]. Concerning different geological and mining conditions, the dominant load can be static, dynamic or both. Due to the abutment pressure, the coal and rock mass next to the longwall panel is under significant stress. The breaking of adjacent overlying rock mass strata can release a large amount of energy, which can lead to a strong, dynamic load when it reaches the roadway. A serious dynamic event (like the rockburst presented in Fig. 13) occurs when the superposition of high static load and dynamic load exceeds the critical load of the common rock. In addition, some areas far from the longwall panel can be under high static stress due to geological disturbances, such as faults, synclines, anticlines, etc. A rock damage or mining work disturbances, like borehole drilling, can cause slight dynamic stress. The superposition of high static load and slight dynamic load

can lead to mine tremors and even a rockburst. It could happen in the area shown in Fig. 16. The effect of damage to a certain roadway after exceeding a critical load in the rock mass can be restrained by high support quality or its construction [9]. Sometimes just the high mechanical properties of coal and rock mass do not allow for a strong seismic event. In any case, the advanced and precise measurement of stress distribution around a longwall panel is of great significance for forecasting and preventing a rockburst hazard. One of the best methods in underground coal mining is the determination of seismic wave velocity anomaly by passive seismic velocity tomography.

In underground coal mining, the geological conditions are complex and the coal and rocks are significantly affected by ground stress, heat, water, etc. The pickup accuracy of p-wave arrival time and ray density is vital to the reliability of tomography results. The given examples indicate that the residual error E_{re} of theoretical and calculated time of the wave propagation in a rock mass is not immutable. It changes with the seismic ray amount used in the tomography. A higher seismic ray density enables a lower convergence value and a higher inversion accuracy. A typical situation of seismic ray density layout inside the longwall panel is shown in Fig. 17. Contour lines show the number of rays on the surface unit (and also in a voxel) – more red, more lines.

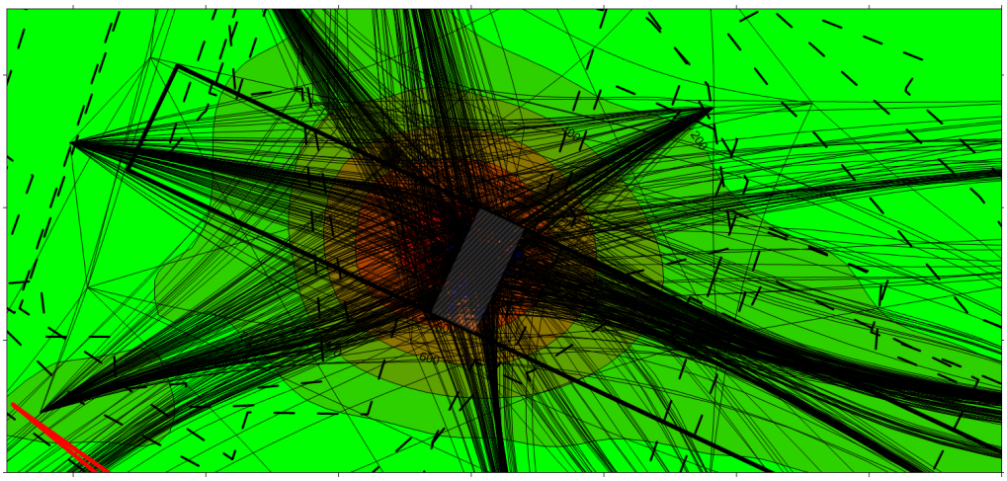

Fig. 17. Example of seismic ray density map in longwall panel

During the mining of a longwall panel, the sensor layout of a micro-seismic monitoring system should be optimised regularly according to the mining schedule, and the panel should be surrounded by more sensors, which would improve the monitoring efficiency and passive tomography results. Moreover, the stress distribution and seismic activity during mining are changeable due to varied geological structures, pressure-relief activities, and others. Therefore, mining-induced tremors that are recorded should be processed in time, and passive seismic tomography should be done periodically. These events stored on a database can then be used to guide pressure-relief activities or other active methods of rockburst hazard prevention. It is worth highlighting a subsequent passive tomography should also be done at a later date to verify the pressure-relief effect.

6. Conclusions and recommendations

- The laboratory tests showed that the increment of elastic wave velocity under loading in different rock types varies from 4% to 21%. The highest velocity increment occurs while a rock structure is the most compacted below the macro-dilatancy threshold, which can be treated as the elastic limit. It is important that even when the rock is damaged, the P-wave velocity is still higher than the initial one and doesn't drop considerably.
- In the elastic deformation stage, the P-wave velocity in coal and rocks is positively related to stress and can be expressed with a power function with a very high determination coefficient. Hence, the high stress and potential rock burst area in coal mines can be determined with the measured seismic velocity and its anomaly.
- The principle and implementation procedure of passive seismic velocity tomography for seismic velocity was introduced. An assessment model of rockburst hazard using velocity anomaly A_n was built. The levels of rockburst hazards for elastic wave velocity anomaly of: 5%, 5-15%, 15-25% and over 25% established as: none, weak, middle and strong, respectively, seem to be sufficiently calibrated in the light of laboratory experiments.
- The case studies verified the feasibility of velocity anomaly calculation for rockburst hazard prediction in coal mines. The observed dynamic phenomena in the field, including tremor layout, coal behaviour in drilled boreholes and post-drilling seismicity, matches the rockburst hazard areas determined by passive tomography.
- For a better application of geotomography results to prevent and control a rockburst hazard, the sensor layout of a micro-seismic monitoring system should be optimised and passive tomography for stress distribution should be carried out periodically according to the mining schedule.

Acknowledgements

It should be noted that the work is supported by the Engineering Laboratory for Safe and Precise Coal Mining of Anhui Province (No.ESCMP202307), Scientific Research Foundation of High-level Talents of Anhui University of Science and Technology (2022yjrc38), National Natural Science Foundation of China (U21A20110) and National Key Research and Development Program of China (2022YFC3004603).

References

[1] P.G. Ranjith, J. Zhao, M.H. Ju, R.V.S. De Silva, T.D. Rathnaweera, A.K.M.S. Bandara, Opportunities and challenges in deep mining: A brief review. Engineering **3** (4), 546-551 (2017). DOI: https://doi.org/10.1016/J.ENG.2017.04.024

[2] P. Małkowski, Ł. Ostrowski, P. Bachanek, Modelling the small throw fault effect on the stability of a mining roadway and its verification by in situ investigation. Energies **10** (12), 2082 (2017). DOI: https://doi.org/10.3390/en10122082

[3] B.T. Shen, Y. Duan, X. Luo, M.D. Werken, B. Dlamini, L. Chen, O. Vardar, I. Canbulat, Monitoring and modelling stress state near major geological structures in an underground coal mine for coal burst assessment. Int. J. Rock. Mech. Min. **129**, 104294 (2020). DOI: https://doi.org/10.1016/j.ijrmms.2020.104294

[4] L.S. Jiang, P. Kong, P.P. Zhang, J.M. Shu, Q.B. Wang, L.J. Chen, Q.L. Wu, Dynamic analysis of the rock burst potential of a longwall panel intersecting with a fault. Rock. Mech. Rock. Eng. **53** (4), 1737-1754 (2020). DOI: https://doi.org/10.1007/s00603-019-02004-2

[5] Y.S. Yang, S.J. Wei, D.M. Zhang, Influence of rock burst and other disasters on stability of surrounding rock of roadway. Geotech. Geol. Eng. **36**, 1767-1777 (2018). DOI: https://doi.org/10.1007/s10706-017-0431-5

[6] P. Małkowski, Z. Niedbalski, A comprehensive geomechanical method for the assessment of rockburst hazards in underground mining. Int. J. Min. Sci. Techno. **30** (3), 345-355 (2020). DOI: https://doi.org/10.1016/j.ijmst.2020.04.009

[7] Q.X. Qi, Y.S. Pan, L.Y. Shu, H.Y. Li, D.Y. Jiang, S.K. Zhao, Y.H. Zou, J.F. Pan, K.J. Wang, HT. Li, Theory and technical framework of prevention and control with different sources in multi-scales for coal and rock dynamic disasters in deep mining of coal mines. J. China. Coal. Soc. **43** (7), 1801-1810 (2018). DOI: https://doi.org/10.13225/j.cnki.jccs.2018.0660

[8] KY. Zhou, L.M. Dou, X.W. Li, S.K. Song, J.R. Cao, J.Z. Bai, X.T. Ma, Coal burst and mining-induced stress evolution in a deep isolated main entry area – A case study. Eng. Fail. Anal. **137**, 106289 (2022). DOI: https://doi.org/10.1016/j.engfailanal.2022.106289

[9] P. Konicek, P. Waclawik, Stress changes and seismicity monitoring of hard coal longwall mining in high rockburst risk areas. Tunn. Under. Sp. Tech. **81** (NOV.), 237-251 (2018). DOI: https://doi.org/10.1016/j.tust.2018.07.019

[10] X.Q. He, W.X. Chen, B.S. Nie, H. Mitri, Electromagnetic emission theory and its application to dynamic phenomena in coal-rock. Int. J. Rock. Mech. Min. **48** (8), 1352-1358 (2011). DOI: https://doi.org/10.1016/j.ijrmms.2011.09.004

[11] J. Li, J.H. Yue, Y. Yang, X.Z. Zhan, L. Zhao, Multi-resolution feature fusion model for coal rock burst hazard recognition based on acoustic emission data. Measurement **100**, 329-336 (2017). DOI: https://doi.org/10.1016/j.measurement.2017.01.010

[12] F.F. Tian, J.S. Lei, X.W. Xu, Teleseismic P-wave crustal tomography of the Weifang segment on the Tanlu fault zone: A case study based on short-period dense seismic array experiment. Phys. Earth. Planet. In. **2020**, 106521 (2020). DOI: https://doi.org/10.1016/j.pepi.2020.106521

[13] W.L. Li, R.Q. Wei, Q.H. Cui, G.H. Li, Y.Z. Zhou, P-wave velocity anomalies atop and in the mantle transition zone beneath the northern South China Sea from triplicated waveforms. J. Asian. Earth. Sci. **197**, 104379 (2020). DOI: https://doi.org/10.1016/j.jseaes.2020.104379

[14] R. Kounoudis, I.D. Bastow, C.S. Ogden, S. Goes, Seismic tomographic imaging of the eastern mediterranean mantle: implications for terminal-stage subduction, the uplift of Anatolia, and the development of the North Anatolian Fault. Geochem. Geophy. Geosy. **21** (7) (2020). DOI: https://doi.org/10.1029/2020GC009009

[15] S. Nakagawa, K.T. Nihei, L.R. Myer, Shear-induced conversion of seismic waves across single fractures. Int. J. Rock. Mech. Min. **37** (1-2), 203-218 (2000). DOI: https://doi.org/10.1016/s1365-1609(99)00101-x

[16] Z.W. Wang, X.B. Li, D.P. Zhao, X.Y. Shang, L.J. Dong, Time-lapse seismic tomography of an underground mining zone. Int. J. Rock. Mech. Min. **107**, 136-149 (2018). DOI: https://doi.org/10.1016/j.ijrmms.2018.04.038

[17] KY. Zhou, L.M. Dou, S.Y. Gong, J.Z. Li, J.K. Zhang, J.R. Cao, Study of rock burst risk evolution in front of deep longwall panel based on passive seismic velocity tomography. Geofluids **2020** (1), 1-14 (2020). DOI: https://doi.org/10.1155/2020/8888413

[18] K. Luxbacher, E. Westman, P. Swanson, M. Karfakis, Three-dimensional time-lapse velocity tomography of an underground longwall panel. Int. J. Rock. Mech. Min. **45** (4), 478-485 (2008). DOI: https://doi.org/10.1016/j.ijrmms.2007.07.015

[19] H. He, L.M. Dou, X.W. Li, Q.Q. Qiao, T.J. Chen, S.Y. Gong, Active velocity tomography for assessing rock burst risks in a kilometer deep mine. Min. Sci. Techno. **21** (5), 673-676 (2011). DOI: https://doi.org/10.1016/j.mstc.2011.10.003

[20] N. Hosseini, K. Oraee, K. Shahriar, K. Goshtasbi, Passive seismic velocity tomography on longwall mining panel based on simultaneous iterative reconstructive technique (SIRT). J. Cent. South. Univ. **019** (008), 2297-2306 (2012). DOI: https://doi.org/10.1007/s11771-012-1275-z

[21] J. Vatcher, S.D. Mckinnon, J. Sjberg, Rock mass characteristics and tomographic data. Rock. Mech. Rock. Eng. **51** (5), 1615-1619 (2018). DOI: https://doi.org/10.1007/s00603-018-1428-y

[22] X. Ma, E. Westman, D. Counter, F. Malek, B. Slaker, Passive seismic imaging of stress evolution with mining-induced seismicity at hard-rock deep mines. Rock. Mech. Rock. Eng. **53** (6), 2789-2804 (2020). DOI: https://doi.org/10.1007/s00603-020-02076-5

[23] R. Ulusay, J.A. Hudson, The complete ISRM suggested methods for rock characterization, Testing and Monitoring. Ankara: ISRM Turkish National Group (2007).

[24] J. Quiñones, J. Arzúa, L.R. Alejano, F. García-Bastante, D. Mas Ivars, G. Walton, Analysis of size effects on the geomechanical parameters of intact granite samples under unconfined conditions. Acta. Geotech. **12**, 1229-1242 (2017). DOI: https://doi.org/10.1007/s11440-017-0531-7

[25] P. Małkowski, L. Ostrowski, J. Brodny, Analysis of Young's modulus for Carboniferous sedimentary rocks and its relationship with uniaxial compressive strength using different methods of modulus determination. J. Sustain. Min. **17**, 145-157 (2018). DOI: https://doi.org/10.1016/j.jsm.2018.07.002

[26] Q.Q. Zhu, D.Y. Li, Z.Y. Han, X.B. Li, Z.L. Zhou, Mechanical properties and fracture evolution of sandstone specimens containing different inclusions under uniaxial compression. Int. J. Rock. Mech. Min. **115**, 33-47 (2019). DOI: https://doi.org/10.1016/j.ijrmms.2019.01.010

[27] R.M. Holt, A.K. Furre, P. Horsrud, Stress dependent wave velocities in sedimentary rock cores: why and why not?. Int. J. Rock. Mech. Min. **34**, 128-44 (1997). DOI: https://doi.org/10.1016/S1365-1609(97)00059-2

[28] F.L. Pellet, G. Fabre, Damage Evaluation with P-Wave Velocity measurements during uniaxial compression tests on argillaceous rocks. Int. J. Geomech.·**7**, 431-436 (2007).
DOI: https://doi.org/10.1061/(ASCE)1532-3641(2007)7:6(431)

[29] W.H. He, Z.L. Chen, H.Z. Shi, C.G. Liu, S.W. Li, Prediction of acoustic wave velocities by incorporating effects of water saturation and effective pressure. Eng. Geol. **280**, 105890 (2020).
DOI: https://doi.org/10.1016/j.enggeo.2020.105890

[30] M. Fathollahy, A. Uromeiehy, M.A. Riahi, Y. Zarei, P-Wave velocity calculation (PVC) in rock mass without geophysical-seismic field measurements. Rock. Mech. Rock. Eng. **54**, 1223-1237 (2021).
DOI: https://doi.org/10.1007/s00603-020-02326-6

[31] J. Dubiński. Seismic method of anticipating assessment of rockburst hazard in hard coal mines. Research Works of Central Mining Institute, extra series, Katowice (in Polish) (1989).

[32] G.K. Ghosh, C. Sivakumar, Application of underground microseismic monitoring for ground failure and secure longwall coal mining operation: A case study in an Indian mine. J. Appl. Geophys. **150**, 21-39 (2018).
DOI: https://doi.org/10.1016/j.jappgeo.2018.01.004

[33] A.Y. Cao, L.M. Dou, W. Cai, S.Y. Gong, S. Liu, G.C. Jing, Case study of seismic hazard assessment in underground coal mining using passive tomography. Int. J. Rock. Mech. Min. **78**, 1-9 (2015).
DOI: https://doi.org/10.1016/j.ijrmms.2015.05.001

[34] H. Navid, Evaluation of the rockburst potential in longwall coal mining using passive seismic velocity tomography and image subtraction technique. J. Seismol. **21** (5), 1101-1110 (2017).
DOI: https://doi.org/10.1007/s10950-017-9654-4

[35] W. Cai, L.M. Dou, S.Y. Gong, Z.L. Li, S.S. Yuan, Quantitative analysis of seismic velocity tomography in rock burst hazard assessment. Nat. Hazards. **75** (3), 2453-2465 (2015). DOI: https://doi.org/10.1007/s11069-014-1443-6

[36] S.Y. Gong, J. Li, F. Ju, L.M. Dou, J. He, X.Y. Tian, Passive seismic tomography for rockburst risk identification based on adaptive-grid method. Tunn. Under. Sp. Tech. **86** (APR.), 198-208 (2019).
DOI: https://doi.org/10.1016/j.tust.2019.01.001

[37] L.M. Dou, W. Cai, S.Y. Gong, R.J. Han, J. Liu, Dynamic risk assessment of rock burst based on the technology of seismic computed tomography detection. J. China. Coal. Soc. **39** (2), 238-244 (2014).
DOI: https://doi.org/10.13225/j.cnki.jccs.2013.2016

[38] G. Mutke, J. Dubiński, A. Lurka, New criteria to assess seismic and rock burst hazard in coal mines. Arch. Min. Sci. **60** (3), 743-760 (2015). DOI: https://doi.org/10.1515/amsc-2015-0049

[39] X.H. Yang, T. Ren, L.H. Tan, A. Remennikov, Effects of water saturation time on energy dissipation and burst propensity of coal specimens. Geomech. Eng. **24** (3), 205-213 (2021). DOI: https://doi.org/10.12989/gae.2021.24.3.205

[40] L.M. Dou, J. He, A.Y. Cao, S.Y. Gong, W. Cai, Rock burst prevention methods based on theory of dynamic and static combined load induced in coal mine. J. China. Coal. Soc. **40** (7), 1469-1476 (2015).
DOI: https://doi.org/10.13225/j.cnki.jccs.2014.1815